Influence of Porosity on Ultra-High Vacuum Gas-Tightness in Cold-Sprayed Aluminum Coatings

Sébastien Weiller, Francesco Delloro, François Willot, Alain Thorel, Michel Jeandin, Cédric Garion

Influence of porosity on ultra-high vacuum gas-tightness in cold-sprayed aluminum coatings

Sébastien Weiller[1], Francesco Delloro[§1], François Willot[1,2], Alain Thorel[1], Michel Jeandin[1], Cédric Garion[3]

Published in: Transport in Porous Media, 144(2), pp. 339–366 (2022).
DOI: 10.1007/s11242-022-01806-3

Abstract

Vacuum chambers used in high-energy particle accelerator experiments are conventionally made of bulk beryllium, which shows significant drawbacks due to cost and toxicity. An alternative solution could be to develop chambers made of polymer-based composites. Since these materials exhibit high outgassing not compatible with an ultra-high vacuum environment, a suitable gas tight coating is required. Cold spray deposition of aluminum can be a solution, provided that the coating behaves as a perfect vacuum barrier. Porosity, especially percolating porous networks, is key to coating gas tightness issues. This work addresses the relationship between porosity and gas-tightness in cold spray coatings. To do so, coatings with different porosity were achieved playing with powder morphology, composition and process parameters. Their gas tightness was evaluated by helium leak tests. Classical microscopy, being essentially a 2D analysis, is strongly limited when dealing with 3D properties as porosity percolation. For this reason, 3D X-ray microtomography images of coatings were obtained and treated by image analysis methods: pores were compared in term of size and shape. Overall porosity properties, including percolation and a homogeneity criterion, were also investigated. Percolating porosity was highlighted for several samples which showed poor gas-tightness properties. The permeability of percolating pore structures was then numerically computed by a fast Fourier transform based method, to quantify the mass flow through the coating. Results of those computations were finally compared to experimental coating leak rate measurements, in an effort to elucidate the link between gas tightness and morphology of the pore space.

Keywords Cold spray; Ultra-High vacuum; Percolation; Porosity; Leak tightness

[*1]Centre of Materials P.-M. Fourt, Mines Paris, PSL Research University, CNRS UMR 7633, BP 87, 91003 Évry, France. [2]Centre of Mathematical Morphology, Mines Paris, PSL Research University, 35 rue S[t] Honoré, 77300 Fontainebleau, France. [3]European Organization for Nuclear Research (CERN), 1, Esplanade des Particules, 1211 Meyrin, Switzerland. [§]Corresponding author. Email: francesco.delloro@minesparis.psl.eu.

1 Introduction

In the LHC (large hadron collider) at CERN (European organization for nuclear research, Geneva, Switzerland), high-energy particle beams travel in vacuum tubes to avoid interactions with gas molecules. Particle collision products are studied by detectors and collisions occurs in the experimental vacuum chambers. Tubular chambers, installed in the heart of these detectors, ensure ultra-high vacuum (UHV in the following) conditions for the beams and require two main characteristics: they must be transparent to secondary particles for data collection on the one hand and, on the other hand, be compatible with UHV environment. In particular, they need to be leak tight and exhibit a low outgassing rate. UHV for CERN application is achieved when the pressure is below 10^{-6} Pa. The chambers in LHC experiments must allow operation in the lower pressure range of UHV, corresponding to a vacuum level in the order of 10^{-8} - 10^{-9} Pa [8].

Bulk beryllium is currently used as the material for UHV experimental vacuum chambers. Its high radiation length (low atomic number), its mechanical properties (high Young's modulus) and its compatibility with UHV make it the best candidate for this application. However, it presents major problems: its scarcity, the difficulty of processing (machining and welding) due to its brittle nature and its high toxicity, in dust or vapor forms, for human health, hamper its use and encourage CERN to consider alternatives [11].

Alternative materials are required to present similar properties to beryllium in terms of transparency to particles and UHV properties, in addition to ensuring the thermo-mechanical resistance of the structure [11]. CFRCs (carbon fibre reinforced composites) are excellent candidates for the substitution of beryllium. They fulfill the criterion of transparency to particles and thermo-mechanical specifications of UHV tubular chambers. The problem lies in their poor UHV performance and, in particular, in their high outgassing rates. This is where cold spray comes into play. This process has demonstrated its versatility of use, allowing the elaboration of coatings with powder/substrate couples of very heterogeneous materials [16]. The potential application in this context would be a lightweight metal coating, thin enough not to compromise the transparency of the assembly to secondary radiation, sprayed on the internal diameter of a CFRC tubular chamber to ensure its gas tightness in UHV conditions. The material chosen for the cold spray coating was aluminum, mainly for its low atomic number. Moreover, it has been used a feed-stock material since the early days of the cold spray process and can be considered today as a well known case. It has been sprayed in its pure form [10] [14] [5] [19], as classical alloys [12] [25] or exotic ones [17], as well as mixed with other powders [20].

Cold spray is based on high velocity impact of micrometer-sized particles, in solid state. A pressurized gas is used as the acceleration medium for the particles. A part of this gas is heated (up to $1200°C$), while another part is fed to the powder dispenser. The two gas streams meet at an injection point, located in a convergent-divergent "De Laval" nozzle. Its shape allows the gas to expand, accompanied by a drop in its pressure and temperature, resulting in its acceleration to supersonic speeds [31]. Particles caught in the gas are then accelerated in a range of speeds between 300 and 1 000 $m.s^{-1}$ [23] [27]. At the impact, particle kinetic energy is transformed into plastic deformation and heat, allowing their adhesion to the substrate. An impact lasts about 100 ns, with deformation rate locally reaching $10^7 - 10^9\ s^{-1}$ [18].

Numerous articles have been published in the whirlwind of cold spray development. However, little have been made regarding gas tightness of cold-sprayed coatings and its relation

with porosity, aside from the work of the authors [28], in which a correlation between gas tightness and porosity in cold spray coatings was highlighted. In [24] the possibility of evaluating gas tightness of parts made by cold spray and SLM (Selective Laser Melting) was formulated, although it has not been done yet. Relevant remarks were given in [15], asserting that gas tightness for UHV conditions might be due to pores at a submicronic scale. Indeed, solid state diffusion can be excluded as a transport route for gas species through coating with a thickness of several hundreds µm. A connected pore network through the whole coating thickness should then be responsible of the eventual gas leakage. The characterization of such a pore network cannot rely on standard 2D metallographic techniques, because the property of interest here - namely the percolation of the pore network - is inherently three-dimensional. A suitable 3D observation technique is X-Ray Microtomography (XMT in the following). In [38], XMT has been applied to titanium cold spray coatings, showing 3D pore networks with a resolution of 2 µm per voxel. In a similar way, in [34], XMT was applied with a resolution of 1.8 µm per voxel to cold-sprayed stainless steel coating. In the latter, the authors stated that the observed porosity was not connected. However, this conclusion is limited to a pore size in the same range of XMT resolution. The presence of finer pores connecting regions in a percolating network cannot be excluded based on these observations. Other studies making use of XMT to characterize porosity in cold spray coatings, such as [26] and [7], made use of a relatively coarse resolution, higher than 1.3 µm per voxel. If a coarser resolution allows imaging a wider volume, this can hinder the observation of small defects, such as sub-micron pores and channels which can be present at particle boundaries.

The present study focuses on the relationship between porosity and gas tightness in aluminum-based cold-sprayed coatings. First, a series of coatings with different porosity levels was produced. These were then characterized by XMT observations and gas leak rate measurements. In particular, it was shown that XMT resolution is a key factor, especially concerning the detection of connected porosity. For this reason, the highest resolution (0.325 µm/voxel) available at the synchrotron XMT line was used. An user-independent image analysis method was developed, to avoid bias when segmenting XMT images. In addition to 3D observations, a finer scale characterization using Transmission Electron Microscopy (TEM) highlighted the presence of sub-micron pore structures. Finally, a flow model was applied to segmented XMT images, in order to numerically evaluate the permeability of the material, induced by the observed pore networks. A comparison of measured and simulated leak rates concluded the work, establishing a quantitative link between percolating porosity networks and gas tightness properties of cold-sprayed materials.

2 Materials and methods

2.1 Powders, cold spray facility, TEM and XMT

Four different feed-stock powders were used in this work: three commercially pure aluminum and one spherical alumina. Coatings were either made of pure Al or Al-alumina composites, as will be described later. Alumina was added to the feed-stock powder mix to obtain denser coatings, taking advantage of its compacting effect shown in previous works, as for example in [20], [33] for aluminum/alumina blends, or in [32] for copper/alumina blends. Powder characteristics are summarized in Table (1). Granulometry stands for particles grain size

Producer	Poudres Hermillon	Ecka Granules	Toyal	Saint Gobain
Country	France	Germany	Japan	France
Reference	ULT02065	AS081	40B5	Under development
Abbreviation	H	E	T	SG
Material	Al 1080	Al 1050	Al 1070	Al_2O_3
Purity	99.8%	99.5%	99.7%	/
Manufacturing	Atom. N_2	Atom. N_2	N.C.	Plasma spheroidization
Granulometry	$[-55, 5\ \mu m]$	$[-11, 45\ \mu m]$	$[-40, 72\ \mu m]$	$[-10, 26\ \mu m]$

Table 1: Powders used for cold spray ("Atom." and "N.C." stand for "Atomisation" and "not communicated").

distribution, and is noted $[-d_{90}, d_{10}]$.

Figure (1) shows SEM-BSE top views of the four above-mentioned powders. The three aluminum powders were chosen for their different morphologies (irregular, spheroidal and almost perfectly spherical). It should be noted that the spheroidal powder presented small satellites. Spherical alumina powder has been obtained by plasma spheroidisation of a crushed powder. The powder cannot be considered as perfectly spherical because several types of defects persist: some particles are still angular, others are hollow or fractured. Moreover, open pores are visible at the surface of some particles.

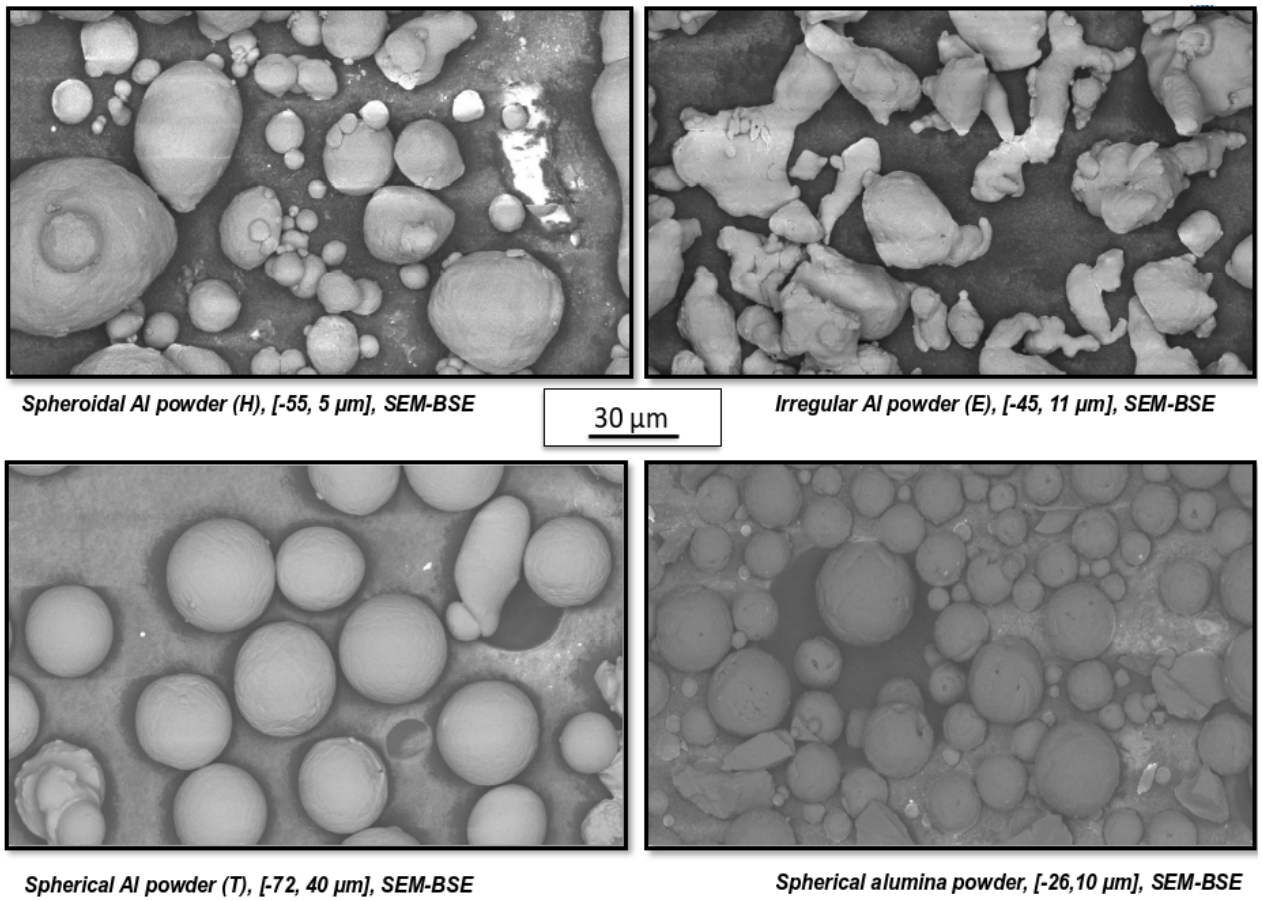

Figure 1: SEM-BSE top view of the four powders.

Substrate material was an aluminum alloy 2017A-T3, in the form of square sheets of size 30x30 mm^2 and 3 mm thick. No surface preparation technique was applied prior to spraying. The nominal composition of the material, according to EN 573-1 [2] is indicated in Table (2).

Cu	Fe	Mn	Mg	Si	Zn	Cr	Al
3.5-4.5	0.7	0.4-1	0.4-1	0.2-0.8	0.25	0.1	rest

Table 2: Nominal composition (atomic %) of aluminum 2017A.

The cold spray system used was a CGT Kinetics 3000. For this equipment, the principal gas pressure ranges from 1 to 3 MPa and its stagnation temperature from 200 to 600°C. Nitrogen was used as spraying gas. The spraying parameters used for this study are summarized in Table (3). The following sample naming convention will be used: powder type (letters as in Table 1), gas pressure (MPa), gas temperature (Celsius), %wt of alumina. For instance, "E 3 300 0" stands for "Ecka powder sprayed at 3 MPa, 300°C without alumina".

Powder	T	E	H
(Pressure [MPa], Temperature [°C], Al_2O_3 content [%wt.])	(3,300,20), (3,300,0), (3,400,20), (2.5,350,20)	(3,300,20), (3,300,0), (3,350,0), (2.5,300,0), (2.5,350,20)	(3,300,20), (3,300,0), (2.5,300,20), (3,350,20), (2.5,350,20)

Table 3: Spraying parameters used in the present study.

As a matter of illustration, Figure (2) shows a SEM-BSE snapshot of E 2.5 350 20.

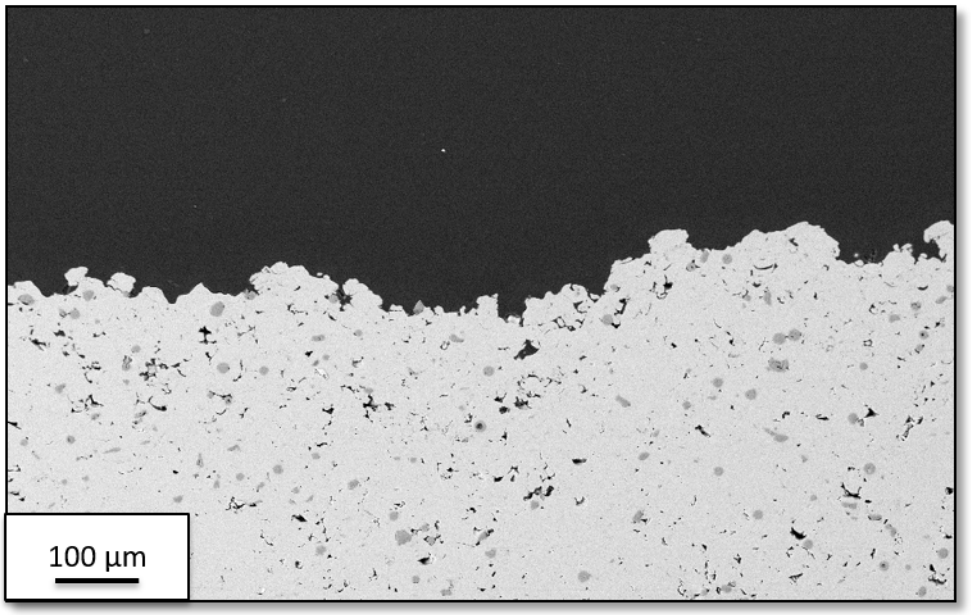

Figure 2: SEM-BSE snapshot of E 2.5 350 20.

XMT observations were carried out at the Soleil synchrotron facility (CEA, Gif-Sur-Yvettes, France). The acquisitions were made on the Anatomix line (Advanced NAnoTOMography and Imaging with coherent X rays) with a parallel beam at 20 keV. The highest resolution possible on this line was chosen, with a voxel size of 0.325 µm. The experimental setup allows to reconstruct a volume of $2048 \times 2048 \times 2048$ voxels, but the area of interest for porosity characterisation was about $1200 \times 1200 \times 500$ voxels. Samples were cut into 500×500 µm^2 rods using a wire saw. They were then placed on 12 mm high sample holders to accommodate the limited Z-stroke of the Anatomix line detector. Figure (3) shows the samples (a) and the XMT line before acquisition (b).

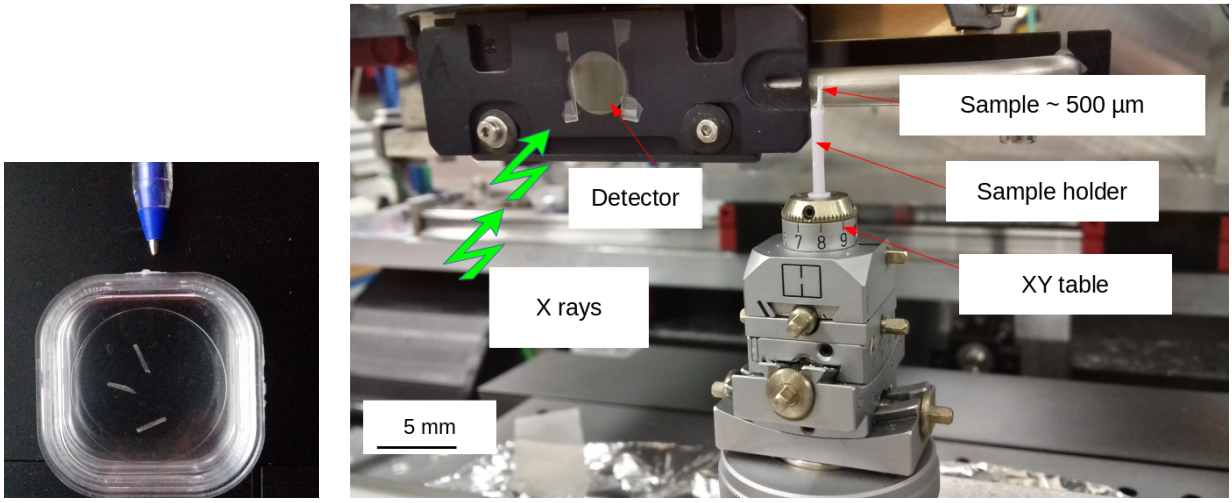

(a) (b)

Figure 3: (a) Photographic image of XTM sample (b) and of the XMT facility.

Smaller scale observations of particle-particle interfaces in the coating were made by TEM on thin blades extracted from the coatings. A SEM equipped with a FIB (Focused Ion Beam) column was used for the preparation of those thin samples, as described in the following. The FIB technology makes it possible to send Ga^+ ions onto a surface. The ions break the bonds between atoms, allowing fine surface machining. To avoid pollution, a detector collects the ions and electrons emitted during the abrasion. Prior to the use of the FIB, a layer of carbon was deposited on the area of interest, to protect it from the effects of Ga^+ ions. The slice was then picked up by a piezo-driven micromanipulator and placed on a copper sample holder. It was refined, by abrasion with the ion beam, to a thickness of about 100 nm. Figure 4 shows a SEM image of a thin slice after refining. The areas of interest are those that will be observed by TEM and present a surface area of about 30 µm^2.

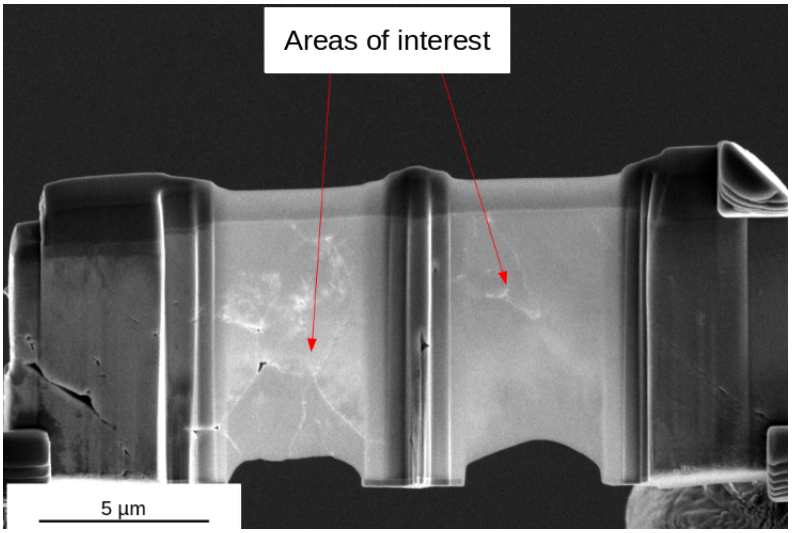

Figure 4: SEM image of a FIB machined thin blade.

2.2 Leak test facility

A leak can be characterised by the rate of material leaving the system. In the case of a liquid, the leak rate corresponds directly to the volume flow rate. This definition deserves a clarification when applied to gases, due to their compressible nature. The leak rate for a gas can be defined as its pressure loss per unit time in a given volume, which corresponds to an energy flow. Its S.I. unit is in $Pa.m^3.s^{-1}$, whereas other units are often used, such as $mbar.l.s^{-1} = 0.1\ Pa.m^3.s^{-1}$. In high-energy physics accelerators, typical helium leak rate acceptance threshold is 10^{-10} $mbar.l.s^{-1}$ or lower. To give an order of magnitude, at this leak rate, a 1 ml gas bubble would take about 317 years to form, for a system subjected to a pressure difference of 1 bar.
In this work, helium, the smallest existing inert gas, mono-atomic, was chosen for a fine characterisation of the tightness. Leak tests were carried out at CERN, using a Phoenix l300i helium mass spectrometry measurement system, by Oerlikon Leybold (Bourg-lès-Valence, France), by the following procedure. The sensitivity of the detector was 5.10^{-12} $mbar.l.s^{-1}$. Vacuum (around 10^{-5} Pa) is created by the turbomolecular pump of the leak detector. The sample to be measured is placed in a sealed holder between the detector and the external environment, charged in helium. The spectrometer measures the amount of helium passing through the sample, allowing the calculation of a leak rate. Figure (5) shows some details of the experimental setup. In the present work, a hood saturated by helium at 1 bar was used as the external environment for leakage measurements. It is also necessary to ensure that the gas tightness of the coating alone is measured, and not that of the coating/substrate pair. A milling and turning procedure (to an accuracy of 0.1 mm) was therefore carried out on the substrate after spraying. In that way, only the gas tightness of the coating is measured.

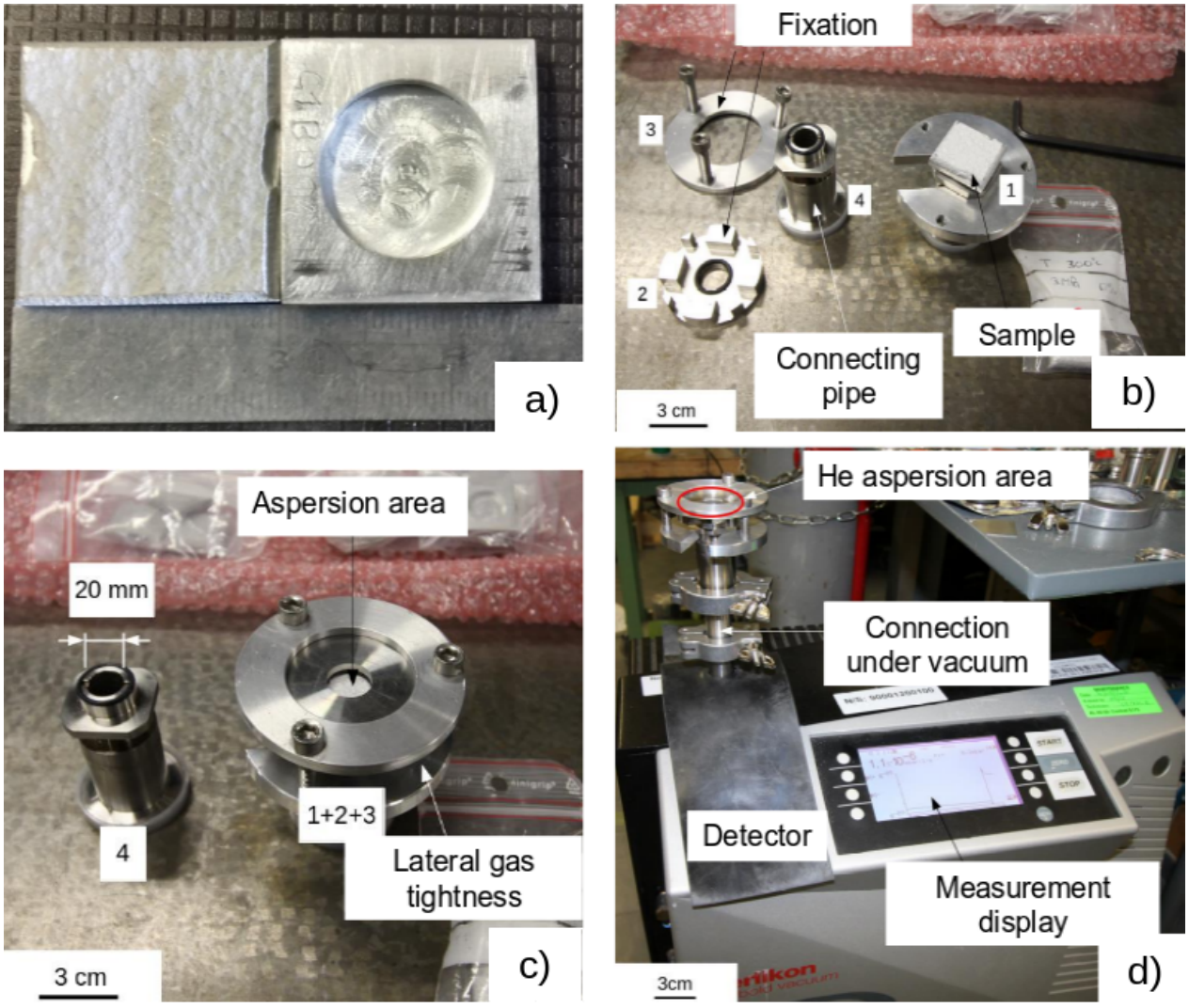

Figure 5: Pictures illustrating the leak test facility. a) Machined sample b) Mounting sample c) Assuring sample lateral gas tightness d) Connecting sample to the leak test facility.

2.3 Numerical methods

2.3.1 Image analysis algorithm

Image segmentation XMT images have been post-treated with the SMIL (Simple Morphological Image Library) Python library [9]. A 3D cross structuring element was chosen for the morphological operations. Particular attention was paid to image segmentation, due to a low contrast of pores and alumina particles with respect to the aluminum matrix, caused by the high beam energy necessary for a voxel size of 325 nm. In addition, the presence of noise in the images was biasing a simple pore-threshold determination. Preprocessing by morphological filtering could eliminate this noise, at the expense of erasing the smallest pores. It was therefore necessary to develop the following segmentation procedure:

(i) The watershed method [4] is first applied on the image to identify the pores. A first coarse thresholding on the base image (called here A) is carried out at a low gray level,

corresponding to the value at 1% of the maximum of the image histogram. This is to create markers to detect the porous phase by watershed. Markers are the connected components of the coarse threshold of A;

(ii) The morphological gradient of A is computed;

(iii) A first segmentation is carried out by watershed, with the markers previously presented and the gradient serving as a ridge line for the water divide. This image is called B;

(iv) Small pores having a lower contrast could not be identified by this procedure. A second method was applied after the watershed. A window size of 10% was found as the best compromise between computational time and contrast increase.

- In an analogous way to a global adaptive thresholding method, the image histogram was calculated within the window and assumed to be Gaussian. A threshold at $\mu - 2\sigma$ allowed to separate the low-contrast porosity (Figure 6c), with μ being the mean and σ the standard deviation.
- The operation is repeated by shifting the window over the entire image. We then obtain N zones $\Sigma_{S1}, ..., \Sigma_{SN}$, containing the segmented low-contrast pores (Figure 7a).
- By thresholding $\Sigma_{S1}, ..., \Sigma_{SN}$ to 0, we reconstruct the final segmented image (Figure 7c).

Figure (6) illustrates the method on a 2D section of a tomographic acquisition.

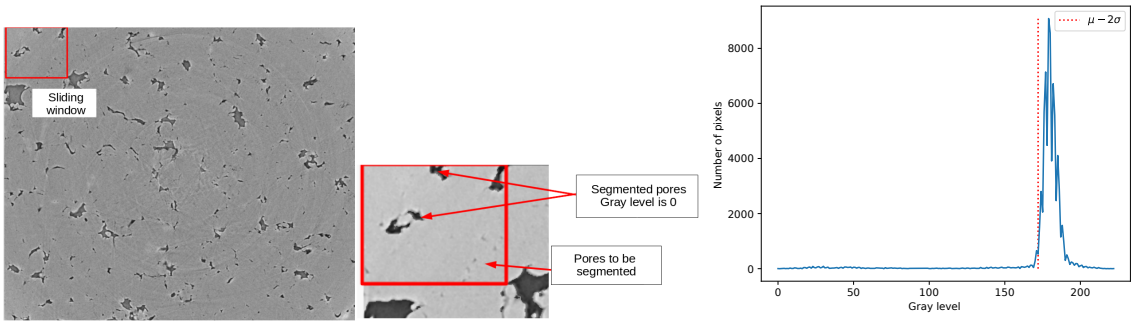

(a) (b) (c)

Figure 6: Low-contrast pore segmentation step: (a) sliding window on A, (b) zoom on Z_{S1}, (c) histogram of Σ_{S1}.

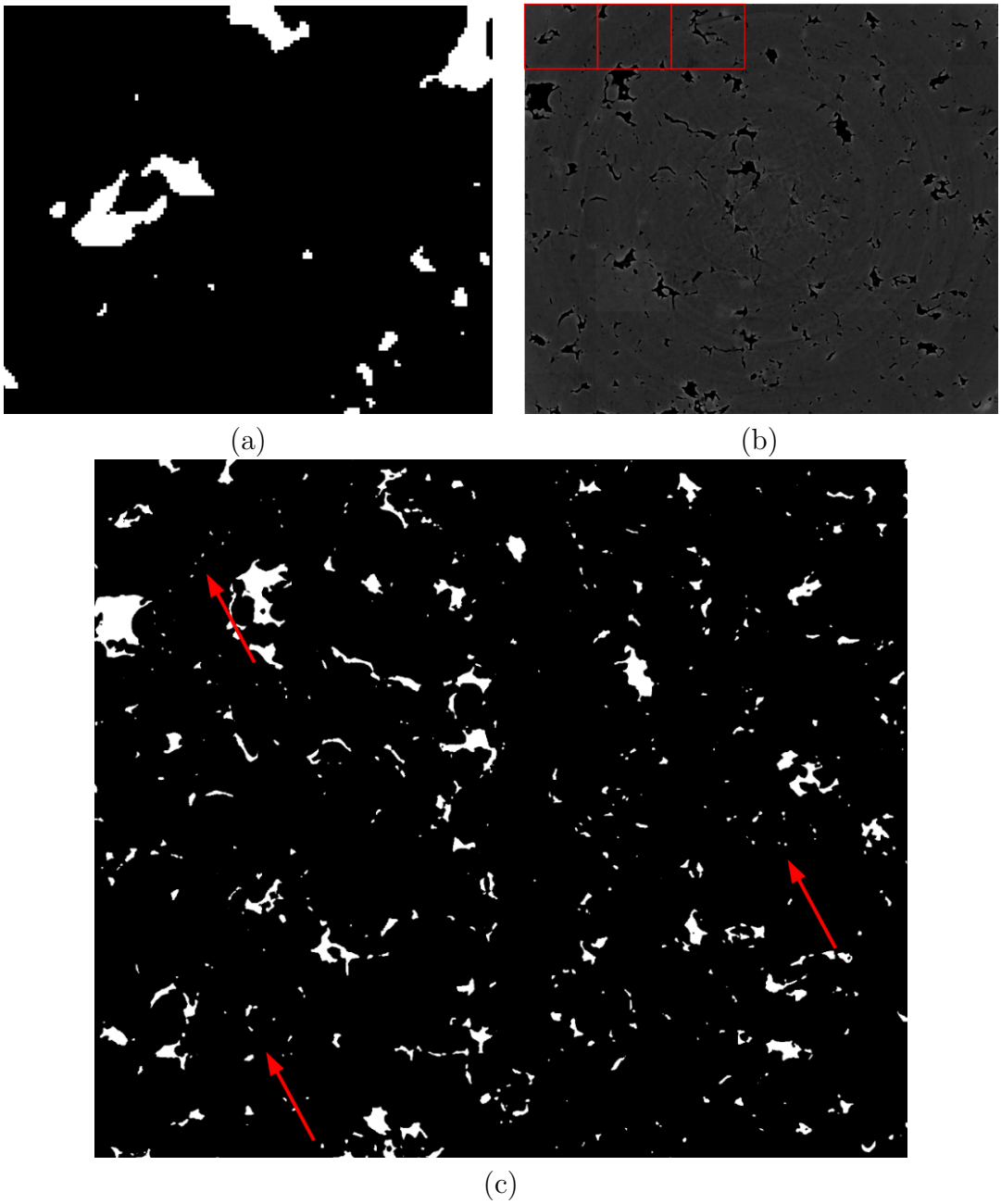

Figure 7: Low-contrast pore segmentation: (a) Σ_{S1} after thresholding, (b) $\Sigma_{S1}...\Sigma_{SN}$ after applying the sliding window method on A (Σ_{S1} Σ_{S2} Σ_{S3} are in red), (c) final segmented image.

Percolation 3D image analysis was used to study the percolation of pores in the microstructure. As a reminder, a phase A percolates in a medium E if there is a connected path, strictly within A, that connects two ends of E. In this study, percolation along the Z axis (spraying direction) was considered. If such pores exist, they span the microstructure from the surface of the coating to the interface with the substrate. One can then expect to find them at the substrate. The search for percolating porosity is carried out on segmented images with the following procedure:

(i) The 3D image is labelled: each connected component is assigned a number (the matrix label is 0);

(ii) The first and last cuts along Z are extracted from the labelled image, called Z_0 and Z_n respectively;

(iii) The histograms of Z_0 and Z_n are calculated, called H_0 and H_n respectively;

(iv) For each value v of H_0, we check if v is in H_n. If this is the case, then the connected component v percolates along the Z axis.

Note that the labelling step depends on the choice of the structuring element. In the present case, no difference was noted between the 3D cross and the cube structuring elements of the SMIL library for the study of percolation.

Flow simulation A numerical simulation of the material flow in the porous structure was developed, to compare with experimental leak rate measurements. In the present work, we assume that the flow regime obeys the Stokes law (details on this point are provided in appendix A). Among the several methods for solving the Stokes equation, the FFT-Stokes developed in [36] was chosen. The simulation stops whenever one of the following conditions is verified:

(i) $\max_{\mathbf{x}\in\mathcal{S}} \|\mathbf{u}(\mathbf{x})\| \leq \eta \max_{\mathbf{x}\in\mathcal{P}} \|\mathbf{u}(\mathbf{x})\|$;

(ii) $\langle\|\mathbf{u}(\mathbf{x})\|\rangle_{\mathbf{x}\in\mathcal{S}} \leq \eta\langle\|\mathbf{u}(\mathbf{x})\|\rangle_{\mathbf{x}\in\mathcal{P}}$,

where η is the required precision, $\mathbf{u}$ is the velocity field, $\mathcal{S}$ and $\mathcal{P}$ the solid and porous phases respectively. The software "morph-hom" [37], implementing the above mentioned FFT-Stokes method, was used to simulate the helium flow in 3D microstructures. On the images used for the simulation, a pressure gradient $\|\nabla p\| = 1$ (a.u.) was applied along the percolation direction (Z axis). Four values of the precision $\eta = 10^{-4}$, $5\,10^{-5}$, 10^{-5} and 10^{-6} were chosen for the study. Simulations were carried out on 12-cores machines with an Intel(R) Xeon(R) E5-2650 v4 processor at 2.20GHz.

Permeability computation Stokes flow, which describes the local behavior of a fluid, can be described by Darcy's law at the macroscopic scale [35] [30]:

$$\langle\mathbf{u}\rangle = -\frac{\boldsymbol{\kappa}}{\mu}\nabla p, \tag{1}$$

where κ denotes the permeability in m^2, $\langle\cdot\rangle$ a mean over the domain and μ the fluid viscosity. The transition from Stokes' equation to Darcy's law then allows the computed permeability alongside the flow axis on the images acquired by tomography to be compared with the permeability measured by the leak test. Accordingly, a simple scalar quantity is enough to assess the role of porosity on the gas tightness of the coatings.

Simulated permeability Permeability alongside the pressure gradient axis is therefore computed as follows:

$$\kappa_Z = \frac{\langle w(x)\rangle\mu}{\|\nabla p\|}, \tag{2}$$

with w the velocity component alongside the Z axis.

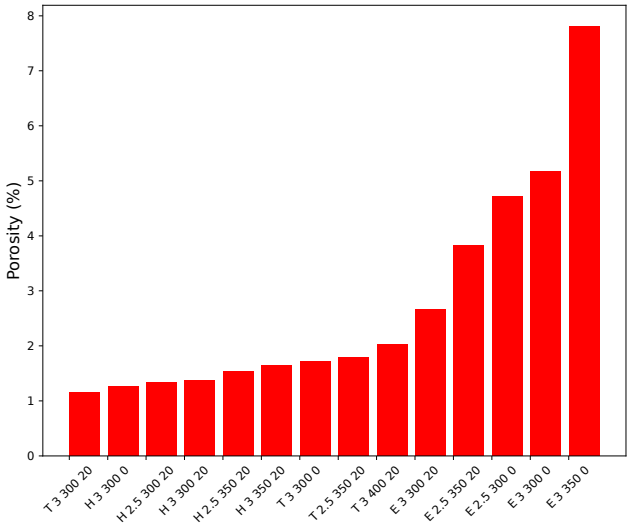

Figure 8: 3D porosity rate versus spraying conditions (naming convention: powder, pressure in MPa, temperature in °C and alumina wt. %).

Measured permeability If Darcy's law applies under the conditions of the leak rate measurement, then the permeability of the coatings can be estimated by taking Equation (1):

$$\kappa_{sample,Z} = \frac{w_{sample}\mu}{g_p}, \qquad w_{sample} = \frac{\Theta}{S_{sample}\Delta P} \tag{3}$$

With $\kappa_{sample,Z}$ the permeability of the sample alongside the percolation axis, Θ the measured leak rate, S_{sample} the area of the sample surface tested (equal to $\simeq 314mm^2$ for a disk of 20 mm diameter), g_p the pressure gradient applied to the sample, and ΔP the pressure difference between the helium-saturated hood and the detector, equal to 1 atm.

3 Results and discussion

3.1 3D porosity

The segmentation method allowed to measure 3D porosity for each sample. Figure (8) shows these result for each spraying condition, varying from 1.1% to 7.8%.

Powder morphology evidently influences porosity, irregular aluminum resulting in the highest porosity rates. It can be noticed that the spraying conditions with 20% wt. alumina led to lower porosity rates. This effect can be explained by the hammering phenomenon of impacting alumina particles on already deposited material, enhancing its compaction. In a general fashion, the addition of hard particles to a powder blend induces the hammering effect and, as a consequence, increases the density of the coating.

Six microstructures out of 14 contained percolating pores. Table 4 shows the corresponding spraying parameters, as well as porosity and a "percolation level", i.e. the ratio between the percolating porosity and the global porosity. The morphological tortuosity is defined as $\min_{(x,y)\in\mathcal{P}} \frac{D_G(x,y)}{D_e(x,y)}$, where $\mathcal{P}$ is the porous phase, D_G and D_e the geodesical and Euclidean

distances respectively. This is then the shortest path between planes Z_0 and Z_n, defined in 2.3.1. The percolation levels varied greatly between microstructures, from 4.8 to 88%. The percolation level was positively correlated with the porosity rate ($R^2 = 0.68$), i.e the more porous the microstructure, the higher the percolation level (see Table 4). Tortuosity was inversely proportional to the porosity of the microstructures studied ($R^2 = 0.64$).

Microstructure	**Percolating pores**	**Porosity rate (%)**	**percolation level (%)**	**Tortuosity (-)**
T 3 300 0	1	1.71	29.3	1.65
E 3 350 0	1	7.80	88	1.30
E 3 300 0	2	5.17	53.7	1.66
T 3 400 20	1	2.03	13.1	2.03
E 2.5 350 20	1	3.82	4.8	N.C
E 2.5 300 0	2	4.71	30.9	1.67

Table 4: Porosity rate, percolation level and morphological tortuosity of the percolating microstructures. N.C stands for "not computable".

Figures 9, 10 and 11 show a 3D representation of the percolating pores, with $X \times Y \times Z$ the size of their bounding box in μm^3. The pores have a two-level structure: small clusters, corresponding to stack defects, are connected by more or less long channels associated to interfacial defects, which occur preferentially along certain particle/particle interfaces. The pore in Figure (9) shows a connection between two large clusters (red circle) through a smaller channel. On Figure (11), one can guess the shapes of the splats, as well as bottleneck shaped pores connecting bigger pore clusters (red arrows).

In order to determine the effect of XMT resolution on coating porosity and its properties (percolation, morphology, isotropy, etc.), an acquisition on the sample E 2.5 300 0 was performed at a lower resolution of 1.33 µm per voxel. Figure (12) shows a comparison of the two resolutions, respectively of 0.33 and 1.33 µm per voxel. The first image will be called HR (High Resolution) in the following and the second one LR (Low Resolution). Pores appear much more clearly on HR images, allowing a more detailed characterization of their morphology and size. Instead, in LR images, they all look spheroidal and many morphological details are hindered. Measured porosity rates were 4.8% and 5.7% for, respectively, HR and LR. Indeed, better resolution came at the expense of the imaged volume size, which was about 10 times smaller in HR than in LR.

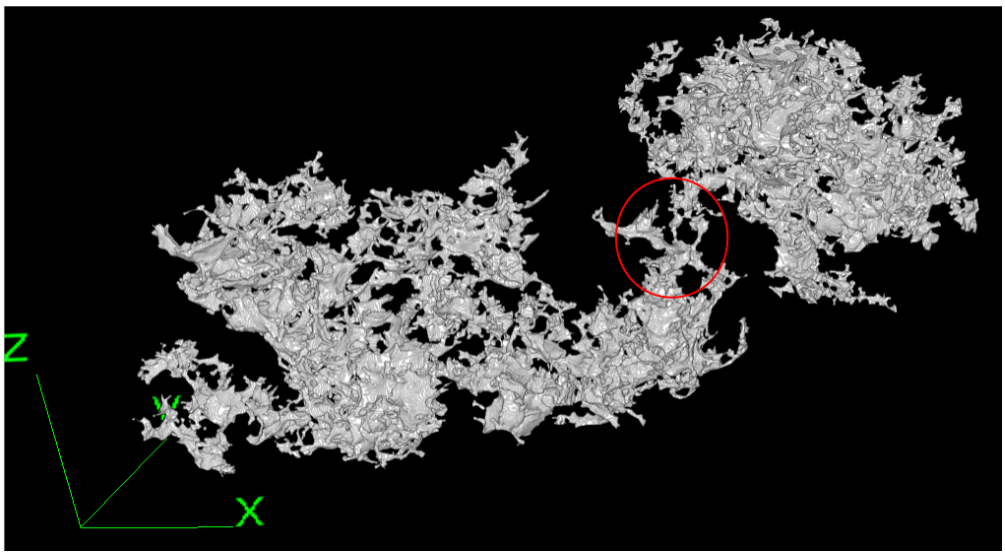

Figure 9: 3D view of the percolating porosity cluster in microstructure E 2.5 300 0. The red circle highlights the small channel connecting the two porous clusters. Domain size: $473 \times 407 \times 162$ μm^3.

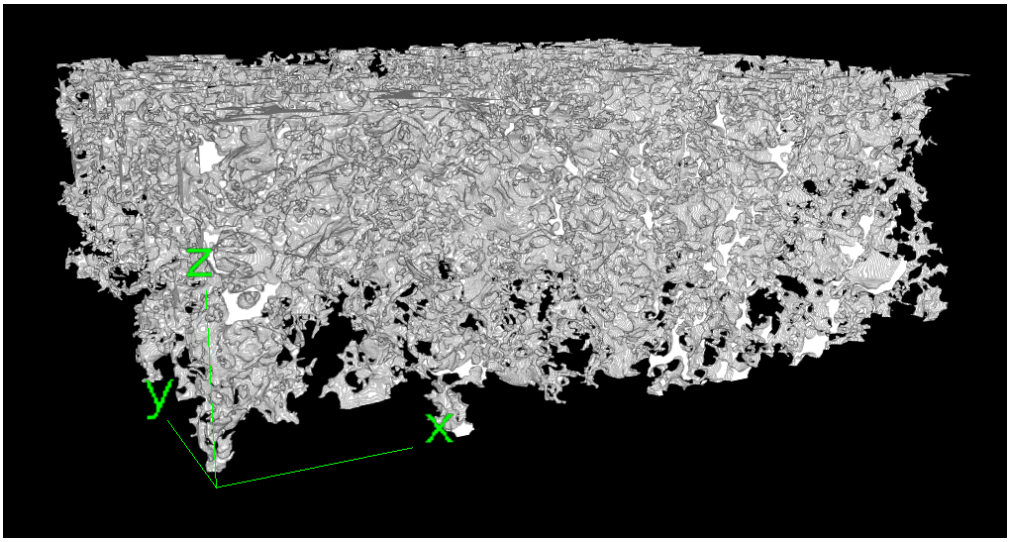

Figure 10: 3D view of the percolating porosity cluster in microstructure E 3 350 0. Domain size: $484 \times 427 \times 162$ μm^3

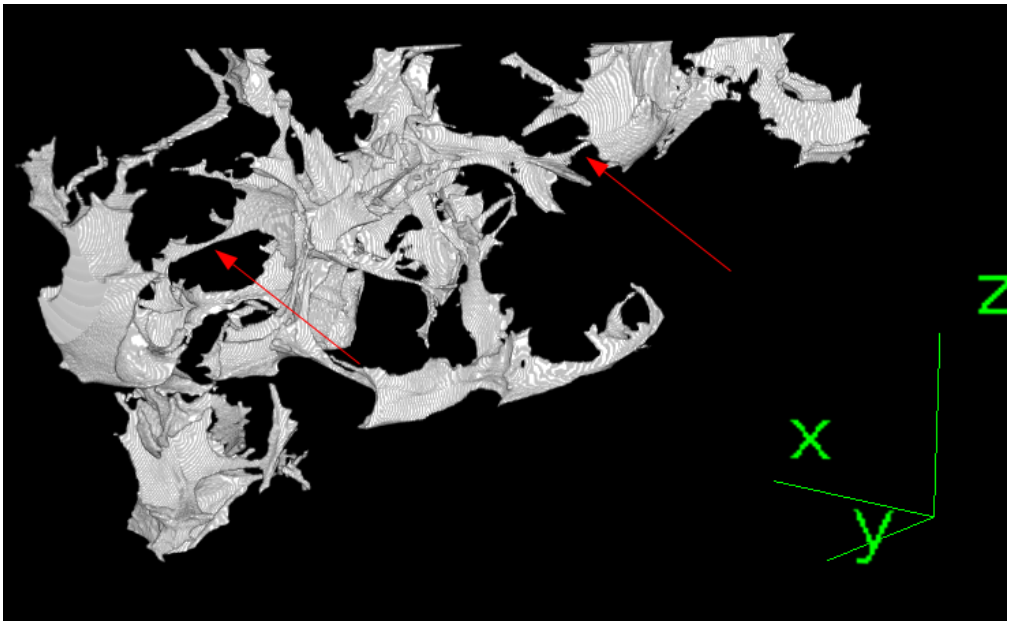

Figure 11: 3D view of the percolating porosity cluster in microstructure T 3 300 0. Arrows indicate bottleneck shaped pores. Domain size: $317 \times 279 \times 162 \mu m^3$.

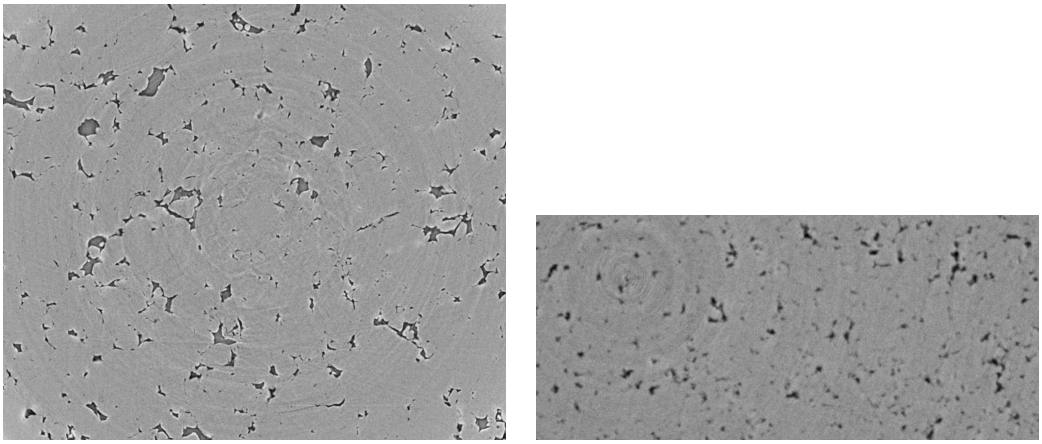

(a) (b)

Figure 12: XMT slice view for E 2.5 300 0 sample for, respectively, HR (a) and LR (b) acquisitions.

The two images were compared in terms of isotropy and stationarity (i.e. translation invariance) of the porous phase. This analysis was performed by calculating the covariance function of the porous phase [29]. Both microstructures show similar covariances, consistently with the hypothesis of isotropy and stationarity of the porous phase [29], as shown in Figure 13, suggesting no influence of the resolution on covariance-related properties.

The analysis of pore grain size, shown in Figure (14), highlights that image resolution has an impact on the shape of the grain size distribution curve. In HR images, percolating porosity occupied a significant portion of the pore volume fraction, as represented by the

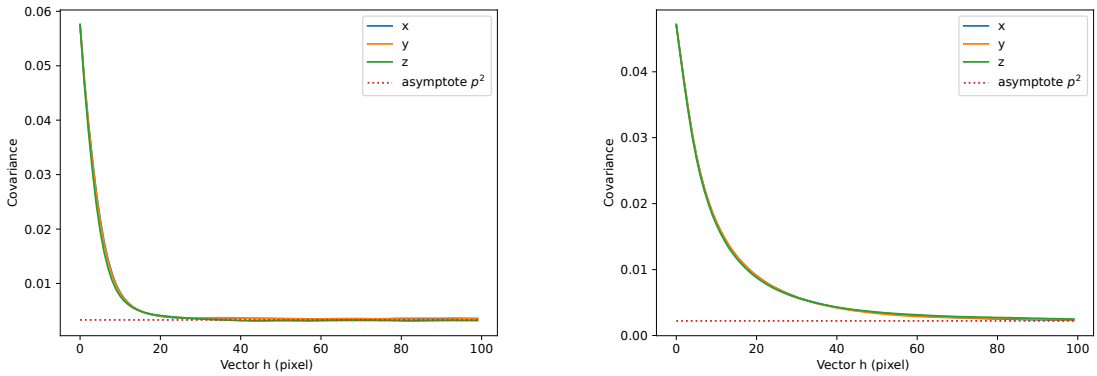

(a) (b)

Figure 13: Covariograms of (a) LR (b) HR.

peak at pore volumes larger than $10^5 \mu m^3$ (Figure 14b). Instead, the LR density distribution shows a Gaussian-like pore volume histogram.

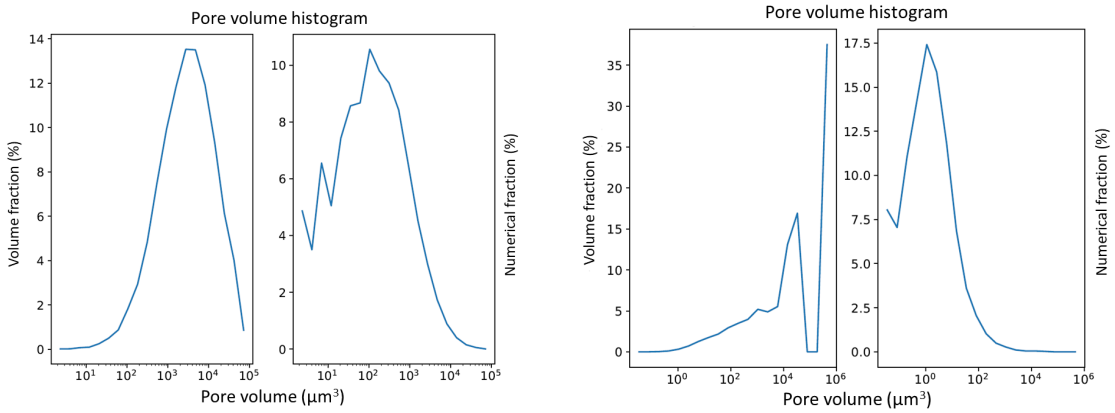

(a) (b)

Figure 14: Pore volume distribution of (a) LR (b) HR.

Pore connectivity is quantified using the percolation algorithm presented in section 2.3. HR shows percolating porosity while LR does not. This analysis illustrates that the voxel size of images is of major importance when it comes to highlighting percolation in cold spray coatings. For a microstructure presenting the same properties (porosity, isotropy, stationarity), a LR analysis hides small pores, which play an important role in connecting larger porous clusters. A voxel size smaller than 1.3 microns is therefore required to identify connected porosity. However, this is at the expense of the volume scanned: the smaller the voxel size, the smaller the volume scanned. This can therefore lead to problems concerning the representativity of the porosity in the microstructure with respect to the volume. A compromise must therefore be made between voxel size and scanned volume. In the case of this study, the smallest voxel size available (325 nm/voxel) was chosen, in order to highlight

Microstructure	Value 1	Value 2	Value 3
H 3 300 20	10^{-10}	/	/
H 3 300 0	10^{-10}	10^{-10}	/
H 2.5 300 20	10^{-10}	10^{-10}	/
H 3 350 20	10^{-10}	10^{-10}	/
H 2.5 350 20	10^{-10}	10^{-10}	/
E 3 300 20	$3\,10^{-5}$	/	/
E 3 300 0	$9\,10^{-3}$	/	/
E 3 350 0	$4\,10^{-3}$	/	/
E 2.5 300 0	$8\,10^{-4}$	/	/
E 2.5 350 20	10^{-9}	$3\,10^{-8}$	/
T 3 300 20	10^{-10}	10^{-10}	10^{-10}
T 3 300 0	$5\,10^{-5}$	$2\,10^{-5}$	/
T 3 400 20	$2\,10^{-8}$	10^{-7}	$7\,10^{-8}$
T 2.5 350 20	10^{-10}	10^{-10}	10^{-10}

Table 5: Measured leak rate values.

as much connected porosity as possible.

3.2 Experimental leak rate and gas tightness

Samples with a measured leak rate up to 10^{-10} mbar.l.s^{-1} are acceptable according to the gas tightness criterion imposed by the final application. Samples with leak rates higher than this value can be, thus, declared leaky. 1 to 3 measurements were made for each microstructure. These values are shown in Table (5), expressed in mbar.l.s^{-1}. They are averaged for the rest of the study.

Three areas can be distinguished in the graph: one where samples are gas tight (porosity $\leq 2\%$), one where gas tightness is gradually lost ($2\% \leq$ porosity $\leq 4\%$) and one with much higher leak rates ($4\% \geq$ porosity). Thus, it can be assumed that a porosity related threshold exists, below which samples are gas tight. On the one hand, all gas-tight samples present low porosity and no percolation at the scale considered. On the other hand, all leaking samples (except E 3 300 20) show percolating porosity on the tomographic acquisitions. In the case of leaking samples, the leak rate can be correlated to the percolation level (see Table 4). When considering percolating microstructures, it can be assumed that the lower the leak rate is, the closer to the threshold the porosity is, at the scale considered (0.325 nm/voxel).
The dispersion in Figure (15) and, in particular, the case of sample E 3 300 20, which constitutes an exception to the general trend, can be considered as an effect of the non-homogeneity of porous structures at small scale. Here, in effect, macroscopic measurements such as the leak rate (measured on the whole sample) were compared to small-scale properties (observed on XMT volumes, approximately 0.02 mm^3). It is, in effect, likely that the small XMT image corresponded to a zone without any percolating pore and that sampling a few hundred microns away would have revealed percolation.
The correlation between porosity and gas tightness is clearly proven: coatings with low porosity are also gas tight and those with high porosity are leaking. Moreover, gas tightness is highly related with the absence of percolating pores. Nevertheless, in the intermediate region

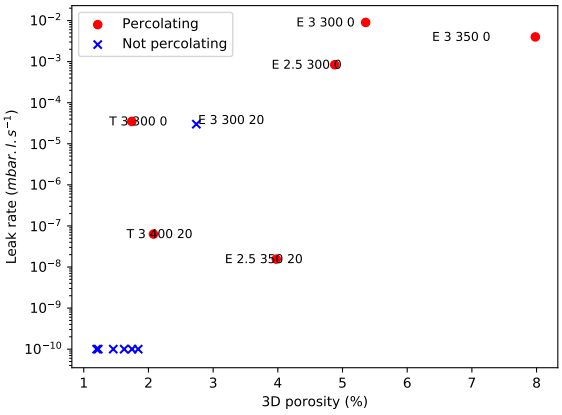

Figure 15: Leak rate versus 3D porosity.

this correlation is less evident and depends on the resolution of XMT images used to assess porosity. As shown earlier, in fact, some samples, not percolating in low-resolution XMT images, revealed a percolating pore network at higher resolution. The porosity detectable only at high resolution seems thus to play a crucial role in the gas tightness of aluminum cold spray coatings.

Another finding of the present work is that, for low to intermediate porosity or percolation microstructures, the size of XMT images may not be sufficient to assess percolation. It has been shown that the percolation property in aluminum cold spray coatings occurs at a scale of less than 1.3 microns. It has also been shown that percolating samples (at this scale) leak. Thus, the detectable porosity below 1.3 microns plays a crucial role in the gas tightness of aluminum cold spray coatings. It can be assumed that for the case E 3 300 20, which has a leak rate of 3 10^{-5} mbar.l.s^{-1}, the sampling for tomography was done in a zone without any percolating pore. When looking at a sample with a similar leak rate that also shows percolation, such as T 3 300 0, it can be seen that the percolating porosity is not homogeneous. It corresponds to the white phase shown in Figure (16). It is likely that observing the same microstructure a few hundred microns away would also not have revealed percolation. This means that for microstructures close to the porosity threshold, the size of the XMT images may not be sufficient enough to assess percolation at a voxel size of 0.325 μm.

For given spraying conditions, no deviation greater than 1 order of magnitude was observed from one measurement to another. The leak rate measurement can therefore be assumed as sufficiently reliable within one order of magnitude and representative of the microstructure considered. Figure 15 shows the values of the leak rates obtained for several spraying parameters, as a function of their 3D porosity. It also indicates whether each acquisition presented one or more percolating pores.

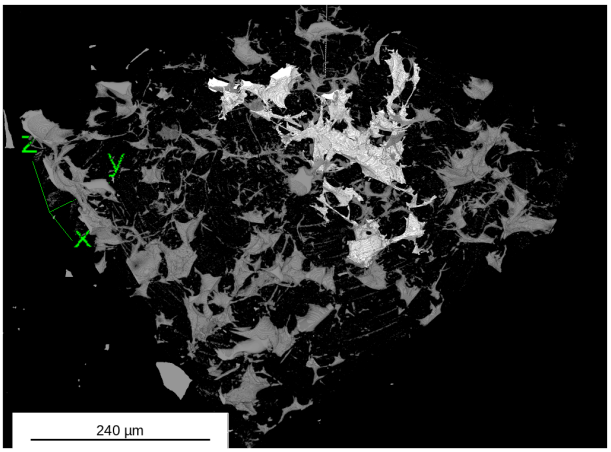

Figure 16: Percolating porosity in T 3 300 0, in white. Non-percolating porosity clusters are in gray.

3.3 Comparison between experimental and computed permeability

The following part of the article presents a modeling approach of gas flow through percolating porosity and the comparison of numerical results with experimental permeability measurements. This analysis will focus, as a consequence, only on leaking samples. Thus, hereafter we focus on 3D microstructures obtained from samples with non-acceptable helium leak rates (regarding CERN application). Regarding permeability, we emphasize that the order of magnitude is most important; in effect, permeabilities of 10^{-14} and 10^{-15} m^2 are often considered equivalent [1].

Figure 17 shows the experimental and computed permeability of the coatings that present percolation, with the corresponding percolation level on the bars. We extrapolate the permeability value using the following empirical power law fit:

$$\kappa(\eta) \sim \kappa(\eta = 0) + a\eta^s, \tag{4}$$

where $\kappa(\eta = 0)$ and the parameters a, s are chosen to fit FFT results (Figure 17, embedded bottom-right graph).

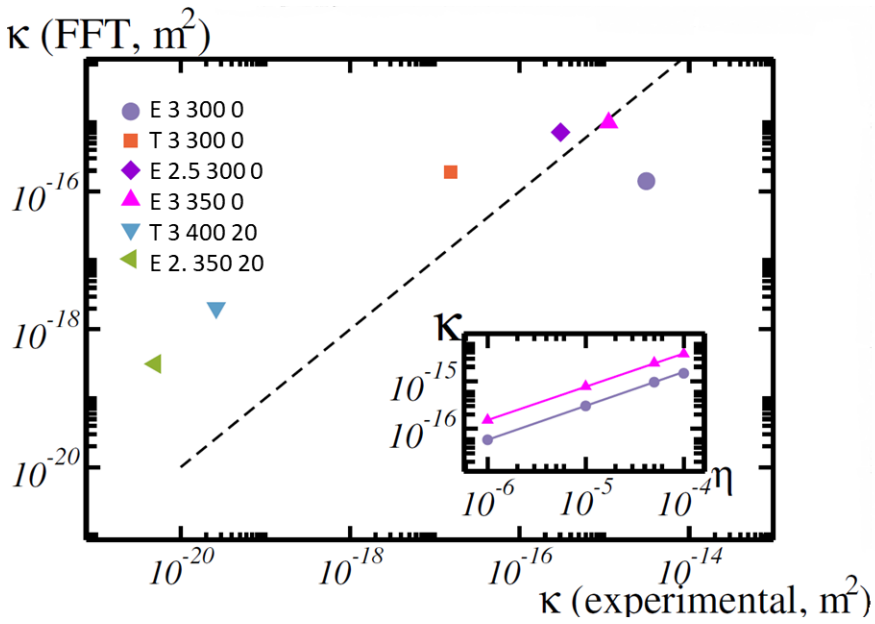

Figure 17: FFT-predicted ($\eta \to 0$) vs. experimentally measured permeability. FFT values are extrapolated from data obtained for various convergence criteria, as illustrated in the embedded graph (bottom-right) for two samples.

Calculated permeabilities deviate from experimental values for T 3 400 20, E 2.5 350 20 and, to a lesser extend, E 3 300 0. They are however in good agreement with that of E 2.5 300 0 and E 3 350 0. For T 3 300, permeability is poorly estimated. The percolation level plays a predominant role in the calculation of the permeability. A too low percolation level, here $< 88\%$, would require the study of several images to correctly estimate the permeability of a cold spray microstructure: a study on a single image is not enough to properly assess simulated permeabilites. This is supported by the calculations on T 3 400 20 and E 2.5 350 20, where the difference between the calculated and measured values varied by 3 to 4 orders of magnitude.

For these two microstructures, it is possible that the percolation level estimated on the tomography images was not representative of that of the whole microstructure. Figure (18) shows the location of the percolating porosity (in white) in the E 2.5 350 20 microstructure. It lies on the edge of the image, it is very elongated along Z and not very extended along the X and Y axes. Non connected porosity (in grey), is homogenous and well distributed, and shows some locally connected cluster, although not percolating along the Z axis. This visualization supports that the measured porosity rate of the images is very close to the porosity threshold, and that it is likely that the percolation level is poorly estimated, leading to the differences shown on the permeability values in Figure (17).

Nevertheless, the calculated permeability values, apart from T 3 400 20 and E 2.5 350 20 (and to a lesser extend E 3 300 0), are not far from the measured values: the permeability of the cold spray coatings can be estimated from the 3D percolating porosity study, supporting the causal nature of the link between porosity at the micro-scale and gas tightness. It is, however, not excluded that smaller porosity may play a role in the gas tightness of the coatings, especially in the absence of bigger percolating porous structures. This could also

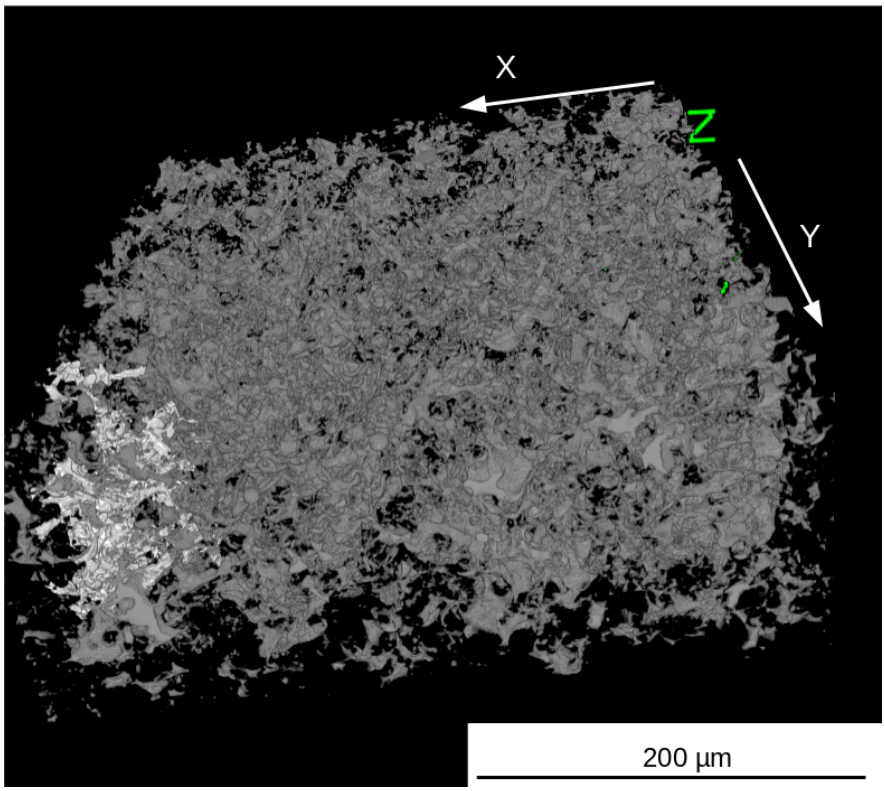

Figure 18: Percolating porosity (white) in E 2.5 350 20. Non-percolating porosity clusters are in gray.

explain why there are such differences between experimental measurements and simulation for some microstructures. The TEM analysis highlighted several features. The E 3 300 0 microstructure is chosen to illustrate the analysis.
On Figure19, a few micropores ($\sim 0.3\mu$m), also detectable by XMT, can be seen. These were found at the interface points between three particles, namely the triple points.

Figure (20a,b) shows an image in STEM-HAADF mode. Impurities could be seen along a grain boundary within the Al3 splat on Figure (20). These were made by elements heavier than aluminum. A deeper chemical analysis, being out of the scope of the present work, was not performed.

The presence of a nanopore, or nanochannel, could also be noticed along the entire length of the interface. Figure (20b) focuses on that area. In the most porous zone, pore thickness was estimated at 45 nm, with an average value of about 10 nm.
An observation by tilting the thin blade, highlighted that this pore might be percolating through it. Such nanochannels, present on the majority of the Al/Al interfaces, could not be detected by XMT. However, the existence of nanochannels forming a porous network percolating throughout the microstructure could play a role in the gas tightness of the coatings: the Van Der Waals radius of a helium atom, used for the leak test, is 140 pm, i.e. two orders of magnitude smaller than the diameter of the nanochannels ($\sim$ 10 to 40 nm).
It is however unlikely that this small-scale porosity is critical on the most permeable samples (leak rate $\geq 10^{-5}$ mbar.l.s^{-1}), as the flow seems to be governed by percolating channels with a diameter larger than half a micron. For microstructures presenting a low percolation level

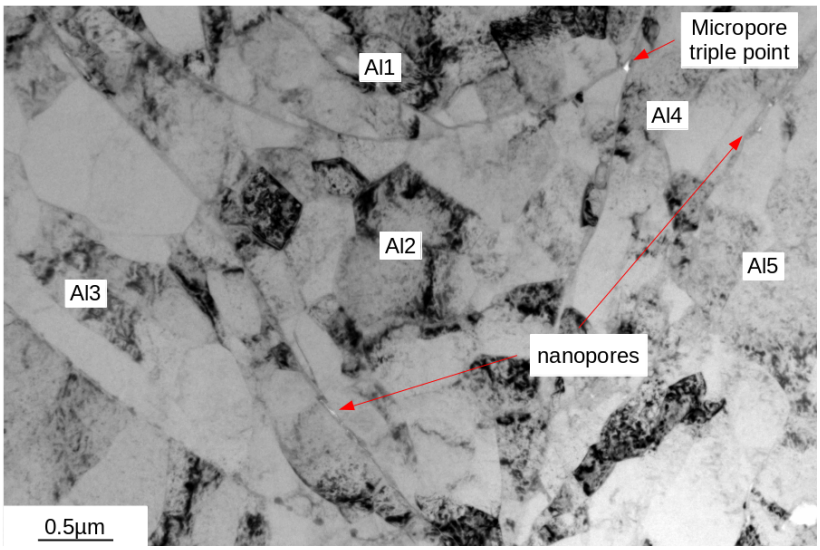

Figure 19: Irregular powder FIB thin blade snapshot. TEM bright field around triple point.

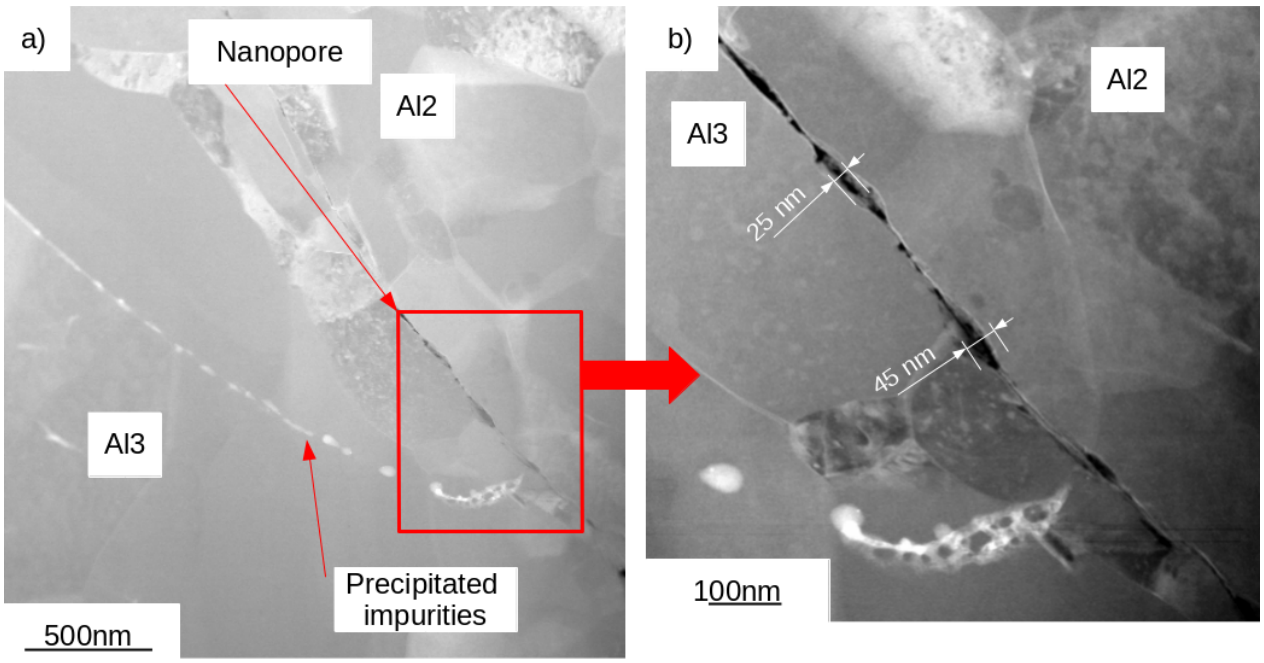

Figure 20: Irregular powder TEM STEM-HAADF snapshots : (a) nanoporosity along the Al2/Al3 interface, (b) Al2/Al3 interface zoom.

(at 0.325 nm/voxel) and low porosity, the presence of percolating nanochannels could play a significant role in coatings gas tightness. However, the modeling approach presented in this article has some limitations at the sub-micron scale. The simulation of gas flow through a percolating nanochannel network would require models that suit better this scale, including for example effects such as molecular flow or slip boundary conditions.

4 Conclusions

X-ray microtomography makes it possible to account for an essential piece of information, percolation, which is not accessible via conventional cross-sectional characterization. Percolating pores have been revealed, with various morphologies. It was shown that acquisitions at 0.33 μm are necessary to highlight this percolation, and that it is likely that the porosity detectable between 0.33 and 1.3 μm plays a critical role in the gas tightness of cold spray coatings.
When a pressure gradient is applied to a microstructure containing porosity at high percolation level, the numerical simulation gives a permeability value similar to that measured experimentally in a helium leak test. In the case of microstructures with low percolation levels ($\leq 15\%$), the influence of the tomographic sampling volume on the permeability estimation is consequent. For the other microstructures (percolation level of 30 to 50%), the calculated average permeability is far from the measured permeability by a factor 10 to 100. Regarding those microstructures, no clear conclusion as to whether their identified percolating porosity is the only cause of their tightness can be made.
It has however been shown that connected porosity in cold spray coatings has a strong bound to their gas tightness properties, and that cold spray is a suitable technology in order to meet CERN high standards regarding UHV chamber.

Several other points, not addressed in the present work, will be studied further. Firstly, although the leak test was repeatable, there was a lack of solid statistics to place error bars on the experimental data. The method of producing the test specimens can be blamed: it was tricky to implement and led to the destruction or detachment of a good part of the coatings.
Spatial resolution is also a major concern for the acquisition of 3D images: it is necessary to have much larger volumes than those acquired in this study, without degrading the resolution. This problem could be mitigated by acquiring a large number of high-resolution images for a given microstructure.
It is also likely that the assumptions leading to the modeling of helium flow in percolating porosity with Stokes equations are too strong or too simplifying. Thus, the modeling of the fluid flow could require to take into account sliding conditions at the walls ($\mathbf{u} \neq \mathbf{0}$), to consider the fluid compressible in some places of the microstructure, or even to use rarefied flow conditions.

Acknowledgments The authors wish to acknowledge to the MATMECA consortium available at the école Centrale/Supélec for the FIB facility.

Declarations

The authors declare that they have no known competing financial interests or personal relationships that could have appeared to influence the work reported in this paper.

A Appendix: Stokes flow conditions

Determining the flow regime of a fluid allows its behavior to be modeled according to the nature of the interactions that predominate and act on its evolution: for this purpose, dimensionless numbers are used involving characteristic quantities of the medium, whether physical (temperature, density, etc.) or geometric (characteristic size). The flow regime can refer to the continuous or discrete nature of the behaviour of a fluid, but also to the behaviour of its flow lines (laminar, transient, turbulent). The simplest flows to consider from a mathematical point of view are Stokes flows: they are continuous, laminar, and in steady state [3].
To decide whether a flow is continuous or molecular, the Knudsen number K_n is used. Depending on its value, the flow is either continuous (the discrete and molecular nature of the fluid is ignored), molecular (the interaction between particles and wall surfaces are prevailing), or rarefied (the interaction between the particles must be governed statistically). This number is defined as follows:

$$K_n = \frac{\lambda}{d} \tag{5}$$

With λ the mean free path of particles and d a representative length of the medium here taken as the inverse of the specific area γ^{-1}. If $K_n < 0.01$, the Navier-Stokes equations can be used to describe the fluid continuously. Although not applicable beyond $K_n = 0.1$, [13] shows that they allow to approximate mean fields, in particular the fluid velocities. For $0.01 < K_n < 0.1$, conditions of fluid sliding on the walls ($\mathbf{v}_{wall}$) should be taken into account. However, in the case of gaseous helium, this effect can be neglected up to $K_n \leq 0.3$ [22] [21].

Figure (21) shows the Knudsen number values for microstructures with percolating porosity, with T = 293 K, P = 101325 Pa and δ = 140 pm, Van Der Waals radius of helium [6].

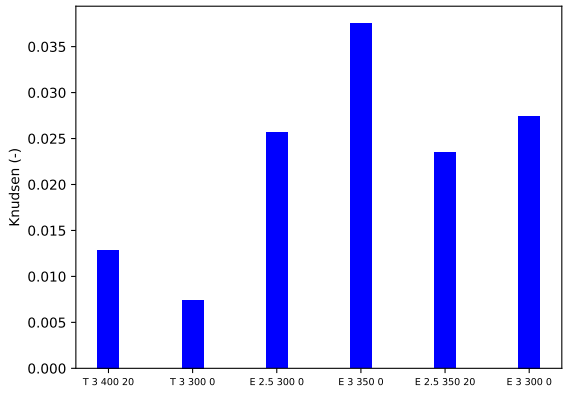

Figure 21: Knudsen number for different microstructures.

Here, $K_n < 0.1$ and is on average equal to 0.022, and varies from 0.0075 to 0.0038, at the limit between the continuous and rarefied flow regimes. Nevertheless, the behavior of the fluid can be described using the Navier-Stokes equations, if we consider average quantities such as the velocity or pressure field [13].
The Naviers-Stokes equations can be simplified. For this purpose, the Reynolds number Re is introduced, which corresponds to the ratio between the inertial term $\rho(\mathbf{u}.\nabla)\mathbf{u}$ and the viscous term $\mu\nabla^2\mathbf{u}$ in a fluid. When $\mathrm{Re} \ll 1$, then the inertial term becomes negligible in front of the viscous term. In this case, the flow is laminar. It is expressed as follows:

$$Re = \frac{\rho v L}{\mu} \tag{6}$$

With ρ the density of the fluid, v the speed of the fluid in the medium, L a characteristic quantity of the medium, here the inverse of the specific surface γ^{-1} and μ the dynamic viscosity.
The velocity was estimated as a function of the thicknesses e and morphological tortuosity τ of the samples. It is assumed that the pore tortuosity of a sample is equal, as a first approximation, to the morphological tortuosity measured on the tomography images. If the sample has two percolating pores, the average of the two tortuosities is taken. The thicknesses were measured with a caliper. Table (6) shows the tortuosities and thicknesses for each sample. In the case of E 2.5 350 20, a tortuosity equal to the average of the tortuosity of the other pores is taken, as the latter could not be measured. As the detector gives a quasi-instantaneous response, 1 s is taken as the value for calculating the velocity.
The speed of helium in a pore is then $v = \frac{e\tau}{1}$.

Sample	**Thickness (mm)**	**Tortuosity (-)**
E 3 300 0	3.3	1.71
T 3 300 0	3.5	2.03
E 2.5 300 0	2.9	2.02
E 3 350 0	3.5	1.30
T 3 400 20	4.1	1.64
E 2.5 350 20	3.1	1.74

Table 6: Thicknesses and tortuosity of the samples for the leak test.

Figure (22) shows the estimated Reynolds numbers for the samples presented in Table 6. All Reynolds values are $\ll 1$, varying in the range $10^{-4} - 10^{-3}$. The inertial term can then be neglected over the viscous term and the flow can be considered as purely laminar.

The flow can also be considered is a steady state. In effect, during the leak experiments, each leak rate measurement was recorded after a certain time interval, so that the value was stable on the detector. Finally, the problem can be reduced to the following equation, corresponding to a Stokes flow:

$$\mu\nabla^2\mathbf{u} = \nabla p - \rho\mathbf{f} \tag{7}$$

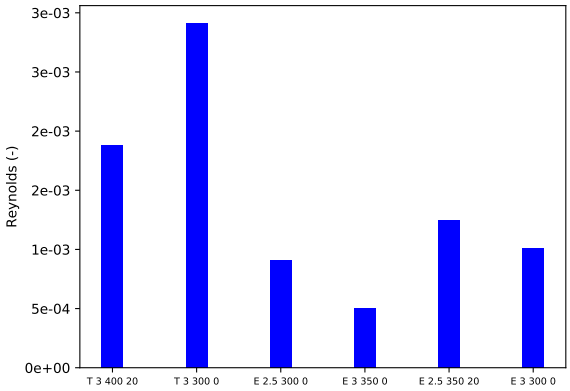

Figure 22: Reynolds number for different microstructures.

References

[1] Bassam Abdallah, François Willot, and Dominique Jeulin. "Stokes flow through a Boolean model of spheres: Representative volume element". In: *Transp. Porous Media* 109.3 (2015), pp. 711–726.

[2] AFNOR. *Aluminium et alliages d'aluminium - Composition chimique et forme des produits corroyés - Partie 1 : système de désignation numérique*. Technical Report NF EN 573-1. Online at `https://www.boutique.afnor.org/norme/nf-en-573-1/aluminium-et-alliages-d-aluminium-composition-chimique-et-forme-des-produits-corroyes-partie-1-systeme-de-designation-numerique/article/789941/fa122749`. Accessed Jul. 15, 2020. 2020.

[3] J.D Anderson. *Fundamentals of Aerodynamics 4th Edition (Book Only)*. McGraw-Hill Science/Engineering/Math, Oct. 2004.

[4] Serge Beucher. "Watershed, hierarchical segmentation and waterfall algorithm". In: *Mathematical morphology and its applications to image processing*. Springer, 1994, pp. 69–76.

[5] Quentin Blochet et al. "Effect of the Cold-Sprayed Aluminum Coating-Substrate Interface Morphology on Bond Strength for Aircraft Repair Application". In: *J. Therm. Spray Technol.* 26.4 (2017), pp. 671–686.

[6] A. Bondi. "van der Waals Volumes and Radii". In: *J. Phys. Chem.* 68.3 (1964), pp. 441–451.

[7] Chaoyue Chen et al. "Microstructure evolution and mechanical properties of maraging steel 300 fabricated by cold spraying". In: *Materials Science and Engineering: A* 743 (2019), pp. 482–493.

[8] G. Engelmann, M. Genet, and W. Wahl. "Vacuum chambers in composite material". In: *Journal of Vacuum Science & Technology A* 5.4 (1987), pp. 2337–2341.

[9] Matthieu Faessel. *Simple Morphological Image Library (SMIL)*. Online at `http://smil.cmm.mines-paristech.fr/wiki/doku.php/licence`. Accessed July 17, 2020. 2019.

[10] Shengqiang Feng et al. *Study on Effects of Heat Treatment on Morphology of Al Coating on the Surface of Mg Alloy by Cold Spray*. The Netherlands: Atlantis Press, 2012.

[11] Cédric Garion. "New Materials for Vacuum Chambers in High Energy Physics". In: *World Journal of Mechanics* 4.3 (2014), pp. 71–78.

[12] Anastasios G. Gavras et al. "Effects of processing on microstructure evolution and fatigue crack growth mechanisms in cold-spray 6061 aluminum alloy". In: *Int. J. Fatigue* 110 (2018), pp. 49–62.

[13] Nicolas G. Hadjiconstantinou. "The limits of Navier-Stokes theory and kinetic extensions for describing small-scale gaseous hydrodynamics". In: *Phys. Fluids* 18.11 (2006), p. 111301.

[14] Mostafa Hassani et al. "Adiabatic shear instability is not necessary for adhesion in cold spray". In: *Acta Mater.* 158.Acta Materialia 158 (2018).

[15] Vincenzo Ierardi et al. "Nano-holes as standard leak elements". In: *Measurement* 58 (2014), pp. 335–341.

[16] Michel Jeandin et al. "Cold spray under the banner of thermal spray in the whirlwind of additive manufacturing". In: *Surf. Eng.* 941 (2018), pp. 1–6.

[17] M. Khomutov et al. "Microstructure of Al–Mg-Sc-Zr alloy cold spray deposits after heat treatment and hot isostatic pressing". In: *J. Alloys Compd.* (2020), p. 157644.

[18] Peter C. King, Saden H. Zahiri, and Mahnaz Jahedi. "Microstructural Refinement within a Cold-Sprayed Copper Particle". In: *Metall. Mater. Trans. A* 40.9 (2009), pp. 2115–2123.

[19] Peter C. King et al. "Aluminium coating of lead zirconate titanate—A study of cold spray variables". In: *Surf. Coat. Technol.* 205.7 (2010), pp. 2016–2022.

[20] P. E. Leger et al. "Multiscale Experimental and Numerical Approach to the Powder Particle Shape Effect on Al-Al2O3 Coating Build-Up". In: *J. Therm. Spray Technol.* 26.7 (2017), pp. 1445–1460.

[21] Abdelhamid Maali, Stéphane Colin, and Bharat Bhushan. "Slip length measurement of gas flow". In: *Nanotechnology* 27.37 (2016), p. 374004.

[22] Jean Maurer et al. "Second-order slip laws in microchannels for helium and nitrogen". In: *Phys. Fluids* 15.9 (2003), pp. 2613–2621.

[23] A. Moridi, S. M. Hassani-Gangaraj, and M. Guagliano. "A hybrid approach to determine critical and erosion velocities in the cold spray process". In: *Appl. Surf. Sci.* 273 (2013), pp. 617–624.

[24] Heiko Neuberger et al. "Fabrication of HCPB breeding blanket components using the additive manufacturing processes of selective laser melting and cold spray". In: *Fusion Eng. Des.* 160 (2020), p. 112026.

[25] Sieglind Ngai et al. "Saltwater corrosion behavior of cold sprayed AA7075 aluminum alloy coatings". In: *Corros. Sci.* 130 (2018), pp. 231–240.

[26] Xiang Qiu et al. “Influence of particulate morphology on microstructure and tribological properties of cold sprayed A380/Al2O3 composite coatings”. In: *Journal of Materials Science & Technology* 44 (2020), pp. 9–18.

[27] François Raletz, Michel Vardelle, and Guillaume Ezo’o. “Critical particle velocity under cold spray conditions”. In: *Surface and Coatings Technology* 201.5 (2006). The 2nd International Meeting on Thermal Spraying, pp. 1942–1947.

[28] Weiller Sebastien et al. *Cold spray as an innovative process to develop ultrahigh vacuum gas-tight aluminum coatings for applications in a large particle collider*. International Thermal Spray Conference, Yokohama, Japan, 2019. Online at `https://www.researchgate.net/publication/335452773_Cold_spray_as_an_innovative_process_to_develop_ultrahigh_vacuum_gas-tight_aluminum_coatings_for_applications_in_a_large_particle_collider`. Accessed Dec 17, 2020.

[29] Jean Serra. “Introduction to mathematical morphology”. In: *Computer Vision, Graphics, and Image Processing* 35.3 (1986), pp. 283–305.

[30] John C. Slattery. “Flow of viscoelastic fluids through porous media”. In: *Industrial & Engineering Chemistry Fundamentals* 13.6 (1967), pp. 1066–1071.

[31] George P. Sutton and Donald M. Ross. *Rocket Propulsion Elements: An Introduction to the Engineering of Rockets*. Hoboken, NJ, USA: John Wiley & Sons Inc, 1992.

[32] Kostoula I. Triantou et al. “Microstructure and tribological behavior of copper and composite copper+alumina cold sprayed coatings for various alumina contents”. In: *Wear* 336-337 (2015), pp. 96–107.

[33] Qiang Wang et al. “Tuning the microstructure and mechanical properties of additive manufactured aluminum matrix composites by cold spray”. In: *Surface and Coatings Technology* 428 (2021), p. 127847.

[34] Yingying Wang, Jérôme Adrien, and Bernard Normand. “Porosity Characterization of Cold Sprayed Stainless Steel Coating Using Three-Dimensional X-ray Microtomography”. In: *Coatings* 8.9 (2018), p. 326.

[35] S. Whitaker. *The Method of Volume Averaging*. Springer Science+Business Media B.V.: Springer Netherlands, 1999.

[36] Andreas Wiegmann. “Computation of the Permeability of Porous Materials from Their Microstructure by FFF-Stokes”. In: *Berichte des Fraunhofer ITWM* 129 (2007). Online at `https://www.researchgate.net/publication/26920688`. Accessed Nov 23, 2022.

[37] François Willot, Bassam Abdallah, and Dominique Jeulin. “The permeability of boolean sets of cylinders”. In: *Oil & Gas Science and Technology–Revue d’IFP Energies nouvelles* 71.4 (2016), p. 52.

[38] Saden Zahiri, Sheridan Mayo, and Mahnaz Jahedi. “Characterization of Cold Spray Titanium Deposits by X-Ray Microscopy and Microtomography”. In: *Microscopy and microanalysis : the official journal of Microscopy Society of America, Microbeam Analysis Society, Microscopical Society of Canada* 14 (2008), pp. 260–6.